Chapter 19
A Temperature-Dependent Viscoelastic Approach to the Constitutive Behavior of Semi-Crystalline Thermoplastics at Finite Deformations

Le Zhang, Bo Yin, Robert Fleischhauer, and Michael Kaliske

Abstract The contribution at hand aims at the formulation of a promising constitutive model for solids exhibiting thermo-viscoelastic characteristics. Temperature dependency and nonlinear creep properties are included into this material formulation. In general, a phenomenological constitutive formulation considering isotropic thermo-viscoelasticity at finite strains is introduced based upon a multiplicative split of the deformation gradient. The evolution equations for the inelastic deformation gradient are introduced in a thermo-dynamically consistent manner. In particular, the present approach focuses on an inelastic incompressibility condition and the principle of maximum of dissipation. The derivation starts from a well-defined HELMHOLTZ energy function, which also includes a volumetric thermal deformation. For simplicity, isotropic thermal conductivity behavior is taken into account. The set of constitutive equations is consistently linearized and incorporated into a NEWTON-type solver. The physical applicability of the present formulation is validated by a promising numerical study, which has also demonstrated favourable numerical stability and robustness.

19.1 Introduction

A special class of polymers with entangled but un-crosslinked macromolecules are thermoplastics. They show significant creep phenomena, when subjected to static mechanical loads, due to the special characteristics of their micro-structure. The

Le Zhang · Robert Fleischhauer · Michael Kaliske
Institute for Structural Analysis, Technische Universität Dresden, 01062 Dresden, Germany,
e-mail: le.zhang@mailbox.tu-dresden.de,robert.fleischhauer@tu-dresden.de,
michael.kaliske@tu-dresden.de

Bo Yin
Ansys Germany GmbH, 99423 Weimar, Germany,
e-mail: liam.yin@ansys.com

H. Altenbach and K. Naumenko (eds.), *Creep in Structures VI*,
Advanced Structured Materials 194, https://doi.org/10.1007/978-3-031-39070-8_19

contribution at hand aims at a thermo-dynamically consistent constitutive modeling of the material behavior of semi-crystalline thermoplastics at finite deformations. The material property, that is especially focused on, is characterized by an elastic and viscous deformation, in order to model the creep behavior of thermoplastics.

The concept of the split of the deformation gradient into volumetric and isochoric parts is applied. The isochoric part is further split into elastic and viscous contributions and the volumetric part is considered to account for thermal and elastic deformations. Based on these multiplicative kinematics, the isochoric elastic right CAUCHY-GREEN deformation tensor is introduced such that it is not influenced by change of temperature. The determinant of the volumetric part of the deformation gradient is used to account for the thermal expansion and stress-inducing volumetric elastic deformations. This kinematic approach is based on the work of [1].

The specific heat capacity of thermoplastics is incorporated into the HELMHOLTZ energy and is assumed to be a material constant. The heat flux vector is assumed to follow FOURIER's law and is a function of the thermal conductivity coefficient for the appropriate thermoplastics, compare [2]. A suitable specific formulation of the HELMHOLTZ energy is introduced, based on [3], consisting of volumetric, isochoric, thermal and latent parts. The energy formulation is used to derive the first PIOLA-KIRCHHOFF stress as well as the external power, which is used to define the change of entropy inside the thermoplastic material. Furthermore, the energy is used to specify the dissipative behavior of the material for considering a change of mechanical into thermal energetic parts, compare [4].

The viscous part of the deformation gradient is driven by its thermodynamic consistent evolution equation. This evolution equation is based on a constitutive viscous flow potential with respect to the viscous intermediate configuration and the respective MANDEL stress. The second internal variable, the hardening strain is driven by the latent part of the HELMHOLTZ energy and its thermodynamic consistent evolution equation. The presented contributions are based on the developments in [3].

All constitutive descriptions and developments are incorporated into a two-field global finite element solver, considering the balance laws of non-linear thermo-inelasticity at finite deformations [2], with respect to the reference configuration. The NEWTON-type solver is based on the consistently linearized field equations for the displacement and the temperature field, which form the global unknown fields. The implicit function theorem is applied to consider the change of these global unknowns, due to a change of the local internal variables, namely the viscous part of the deformation gradient and the hardening strains. All computational developments and constitutive descriptions are successfully validated by a representative numerical study, where the experimental creep data for polyoxymethylene (POM) at 60°C, taken from [5], is used to identify the introduced material constants.

The framework of this paper is outlined as follows. In Sect. 19.2, the preliminaries of the finite thermo-viscoelasticity are introduced, which pay particular attentions to the basic kinematics and the multiplicative decomposition of the total deformation gradient. In Sect. 19.3, a brief overview of the constitutive framework is summarized, including the HELMHOLTZ free energy and the nonlinear creep law. In the sequel, a

representative numerical example is studied in Sect. 19.4, consisting of both stress-controlled and strain-controlled loading conditions. Sect. 19.5 closes the paper by summarizing the present work and proposing future perspectives.

19.2 Preliminaries of the Finite Thermo-Viscoelasticity

This section depicts the fundamental theoretical background of the constitutive framework of the isotropic thermo-viscoelasticity. To classify the deformation process, let $\mathcal{B}_0$ be the solid body in the reference configuration as a subset of the EUCLIDEAN space $\mathcal{B}_0 \subset \mathbb{R}^3$ at $t_0 \in \mathcal{T} \mid \mathcal{T} \subset \mathbb{R}_+$. For each material point P_{t_0} of $\mathcal{B}_0$, its position vector is $\boldsymbol{X} \in \mathcal{B}_0$. At time $t \in \mathcal{T}$, the current configuration is denoted as $\mathcal{B}_t$ and the corresponding material point P_t has a position vector $\boldsymbol{x} \in \mathcal{B}_t$. The mapping $\boldsymbol{\varphi}_t : \mathcal{B}_0 \times \mathcal{T} \rightarrow \mathbb{R}^3$ denotes the motion of the solid domain at the time interval $\mathcal{T}$. The motion $\boldsymbol{\varphi}_t$ is a non-linear and bijective mapping, reading $\boldsymbol{\varphi}_t : \boldsymbol{X} \mapsto \boldsymbol{x} = \boldsymbol{\varphi}_t(\boldsymbol{X})$. The deformation gradient $\boldsymbol{F}$ is now defined as

$$\boldsymbol{F}(\boldsymbol{X}) := \operatorname{Grad}\left(\boldsymbol{\varphi}_t(\boldsymbol{X})\right) = \frac{\partial \boldsymbol{\varphi}_t(X)}{\partial \boldsymbol{X}} = \boldsymbol{g}_i \otimes \boldsymbol{G}^i \tag{19.1}$$

having a determinant $J(\boldsymbol{X}) := \det(\boldsymbol{F})$. The basis vectors $\boldsymbol{G}_i$ and $\boldsymbol{g}_i$ are defined with respect to the reference and the current configuration, respectively.

The absolute temperature for a point of $\mathcal{B}_t$ is denoted as $\theta \geq 0\,\mathrm{K}$. Furthermore, it is common to denote the reference temperature for a material point of $\mathcal{B}_0$ as θ_0 and define the change of temperature ϑ as

$$\vartheta := \theta - \theta_0 \,. \tag{19.2}$$

As a convention, the temperature is transferred into units of Kelvin [K] instead of Celsius [°C] or Fahrenheit [°F], which naturally enables that temperature parts of the HELMHOLTZ energy can be introduced by a logarithmic form due to the strict positiveness.

For a finite thermo-viscoelastic formulation, the deformation gradient $\boldsymbol{F}$ is split into the thermal and viscoelastic parts

$$\boldsymbol{F} = \boldsymbol{F}^{\vartheta}\, \boldsymbol{F}^{ve}. \tag{19.3}$$

The thermal part of the deformation is constitutively assumed to be of purely volumetric nature, so that an increase of temperature ensures an increase of the volume of the solid body and vice versa. Here, the volumetric thermal expansion is modeled by

$$\boldsymbol{F}^{\vartheta} = \left(J^{\vartheta}\right)^{\frac{1}{3}} \mathbf{1}, \qquad \text{where} \qquad J^{\vartheta} = \exp(3\,\alpha_t\,\vartheta)\,, \tag{19.4}$$

where $\mathbf{1}$ is the identity tensor and α_t denotes the isotropic thermal expansion coefficient. Based on [4], herein an exponential form of the thermal expansion is introduced.

The non-thermal part

$$\boldsymbol{F}^{ev} = (J^{ev})^{\frac{1}{3}}\,\bar{\boldsymbol{F}}^{ev}$$

can also be further split based on a volume preserving formulation, namely

$$\bar{\boldsymbol{F}}^{ev} = \bar{\boldsymbol{F}}^{e}\,\bar{\boldsymbol{F}}^{v} \tag{19.5}$$

for the elastic and viscous parts; see e.g. [1, 6–10]. Therefore, the determinant of deformation gradient J satisfies $J = J^{\vartheta} J^{ev}$.

The viscous part of the deformation $\bar{\boldsymbol{F}}^{v}$ describes the irreversible and inelastic part of the total isochoric deformation. This portion can evolve e.g. due to the creep law, leading to micro-structural rearrangements of the material and, thus, to dissipation and temperature changes. Once $\bar{\boldsymbol{F}}^{v}$ evolves, the incompressibility condition

$$\det\left(\bar{\boldsymbol{F}}^{v}\right) = J^{v} = 1 \;\forall\; \bar{\boldsymbol{F}}^{v} \tag{19.6}$$

has to be ensured for most of the materials, especially for metals, see [11]. The time derivative of inelastic deformation gradient is defined by

$$\dot{\bar{\boldsymbol{F}}}^{v} = \bar{\boldsymbol{L}}^{v}\,\bar{\boldsymbol{F}}^{v}\,, \tag{19.7}$$

where $\bar{\boldsymbol{L}}^{v}$ is the rate of deformation. The elastic part is defined by

$$\bar{\boldsymbol{F}}^{e} = \bar{\boldsymbol{F}}^{ev}\,\bar{\boldsymbol{F}}^{v^{-1}}\,. \tag{19.8}$$

Using Eq. (19.8), the deformation measure

$$\bar{\boldsymbol{C}}^{e} = \bar{\boldsymbol{F}}^{e^{T}}\boldsymbol{g}\bar{\boldsymbol{F}}^{e} = \bar{\boldsymbol{F}}^{v^{-T}}\bar{\boldsymbol{F}}^{T}\boldsymbol{g}\bar{\boldsymbol{F}}\bar{\boldsymbol{F}}^{v^{-1}} \tag{19.9}$$

is introduced as a function of the current metric tensor $\boldsymbol{g}$, which represents a key kinematic quantity for defining specific constitutive equations.

Furthermore, the heat flow q_n out of the surface $\partial\mathcal{B}_t$ of the current configuration can be expressed as $q_n =: \boldsymbol{q}\cdot\boldsymbol{n}$, where $\boldsymbol{q}$ denotes the spatial heat flux through a point $\boldsymbol{x} \in \partial\mathcal{B}_t$ and $\boldsymbol{n}$ is the current outward normal at the observed point, see Fig. 19.1. The spatial heat flux vector $\boldsymbol{q}$ at point $\boldsymbol{x} \in \mathcal{B}_t$, describing the heat conduction inside of the solid body, is assumed to follow FOURIER's law

$$\boldsymbol{q} = -\frac{k}{J}\mathrm{grad}(\vartheta)\,, \tag{19.10}$$

where k is a material constant. Eq. (19.10) sufficiently describes the spatial heat conduction phenomena by the current state of the temperature gradient $\mathrm{grad}(\vartheta)$. Additionally, the conductive dissipation

$$\mathcal{D}_{con} := -\frac{1}{\theta}\boldsymbol{q}\cdot\mathrm{grad}(\vartheta)$$

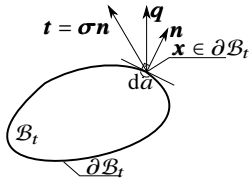

Fig. 19.1 Schematic depiction of the boundary $\partial\mathcal{B}_t$ of the current configuration and its normal $\boldsymbol{n}$ at point $\boldsymbol{x}$ as well as tractions $\boldsymbol{t}$ and heat flux $\boldsymbol{q}$

is also fulfilled.

19.3 Constitutive Formulation of Finite Thermo-Viscoelasticity

19.3.1 Helmholtz Energy

In order to define the isotropic thermo-viscoelastic material in a systematic manner, the HELMHOLTZ energy ψ is particularly defined herein, reading

$$\psi = \psi^e_{vol} + \psi^e_{iso} + \psi^{\vartheta} \,, \tag{19.11}$$

where ψ^e_{vol} denotes the volumetric part from both the elastic deformation and the temperature changes. ψ^e_{iso} represents the isochoric energy density. Additionally, a pure thermal contribution ψ^{ϑ} captures the change of free energy due to any change of temperature. The volumetric and isochoric part of Eq. (19.11) take the definition of [12, 13], reading

$$\rho_0\psi^e_{vol}(J, J^{\vartheta}) = \frac{\kappa}{2}\cdot\ln(J^{ev})^2, \qquad \text{and} \qquad \rho_0\psi^e_{iso}(\bar{\boldsymbol{C}}^e) = \frac{\mu}{2}(\bar{I}_1 - 3), \tag{19.12}$$

respectively, noting, $\bar{I}_1 = \text{tr}\,(\bar{\boldsymbol{C}}^e) = \delta_{ij}\bar{\boldsymbol{C}}^e_{ij}$. The thermal part $\rho_0\psi^{\vartheta} = \rho_0\psi^{\vartheta}(\vartheta)$ is defined as

$$\rho_0\psi^{\vartheta}(\vartheta) = -\rho_0 c\left(\theta\ln\left(\frac{\theta}{\theta_0}\right) - \vartheta\right) + C(\vartheta) \,. \tag{19.13}$$

The corrector function $C(\vartheta)$ is required in order to ensure the assumed constant heat capacity at constant deformation. The specific heat capacity c is defined by

$$\rho_0 c := -\theta\frac{\partial^2\rho_0\psi}{\partial\vartheta\partial\vartheta} = -\theta\frac{\partial^2\rho_0\psi^e_{vol}(J, J^{\vartheta})}{\partial\vartheta\partial\vartheta} - \theta\frac{\partial^2\rho_0\psi^{\vartheta}(\vartheta)}{\partial\vartheta\partial\vartheta} \tag{19.14}$$

and determines the temperature-dependent part of the HELMHOLTZ energy by

$$\frac{\partial^2\rho_0\psi^{\vartheta}(\vartheta)}{\partial\vartheta\partial\vartheta} = -\frac{\partial^2\rho_0\psi^e_{vol}(J, J^{\vartheta})}{\partial\vartheta\partial\vartheta} - \frac{\rho_0 c}{\theta} \,. \tag{19.15}$$

An integration over the temperature domain together with the use of the constraints $\partial\theta\psi^{\vartheta}(\vartheta=0):=0$ and $\partial\theta\theta^2\psi^{\vartheta}(\vartheta=0):=0$ as well as considering $\theta=\theta_0\ \forall\ \vartheta=0$ would yield the specific formulation of ψ^{ϑ} and $C(\vartheta)$, respectively.

Following [14], the Cauchy stress tensor $\boldsymbol{\sigma}$ and the Kirchhoff stress tensor $\boldsymbol{\tau}$ are given by

$$\boldsymbol{\sigma}=2\rho\frac{\partial\psi}{\partial\boldsymbol{g}}=\frac{2}{J}\frac{\partial\rho_0\psi}{\partial\boldsymbol{g}}=\frac{1}{J}\boldsymbol{\tau}\ , \tag{19.16}$$

where ρ is the current density and $\boldsymbol{g}$ the current metric tensor. According to Eq. (19.11), the Cauchy stresses are additively split into volumetric and isochoric parts, reading

$$\boldsymbol{\sigma}_{\mathrm{vol}}=\frac{1}{J}\left[\kappa\ln(J^{ev})\boldsymbol{g}^{-1}\right]\ ,\qquad\text{and}\qquad\boldsymbol{\sigma}_{\mathrm{iso}}=2\mu J\frac{\partial\bar{I}_1}{\partial\boldsymbol{g}}\ . \tag{19.17}$$

The external power

$$\rho w_{\mathrm{ext}}:=\rho\theta\left(2\frac{\partial^2\psi}{\partial\boldsymbol{g}\partial\vartheta}\right):\boldsymbol{d}=\theta\frac{\partial\boldsymbol{\sigma}}{\partial\vartheta}:\boldsymbol{d}=\theta\frac{\partial\boldsymbol{\sigma}}{\partial\vartheta}:\mathrm{sym}\boldsymbol{l}\ , \tag{19.18}$$

where $\boldsymbol{l}=\dot{\boldsymbol{F}}\boldsymbol{F}^{-1}$ is the spatial velocity gradient and $\boldsymbol{d}$ its symmetric part, influences the change of entropy per time. After the specification of the Helmholtz energy, ρw_{ext} takes the form

$$\rho w_{\mathrm{ext}}=\frac{\kappa\theta}{J}\left[\frac{1}{J^{ev}}\frac{\partial J^{ev}}{\partial\vartheta}\right]\boldsymbol{g}^{-1}:\mathrm{sym}\boldsymbol{l} \tag{19.19}$$

and represents the amount of energy that changes the temperature at $\boldsymbol{x}$, due to an arbitrarily applied deformation rate. This part of the entropy change is a function of the volumetric energy, since temperature changes only affect the changes in volumetric deformation of most materials.

The internal power is expressed as

$$\rho w_{\mathrm{int}}:=\rho\left(\frac{\partial\psi}{\partial\bar{\boldsymbol{F}}^{v}}-\theta\frac{\partial^2\psi}{\partial\bar{\boldsymbol{F}}^{v}\partial\theta}\right):\dot{\bar{\boldsymbol{F}}}^{v}\ , \tag{19.20}$$

which models any change of temperature at $\boldsymbol{x}\in\mathcal{B}_t$ due to the evolution of internal variables in an irreversible manner, whenever $\dot{\bar{\boldsymbol{F}}}^{v}\neq\boldsymbol{0}$. Eq. (19.19) captures the reversible change of temperature at any deformation rate, while Eq. (19.20) can be interpreted as an underlying ground state temperature change response. If $\dot{\bar{\boldsymbol{F}}}^{v}=\boldsymbol{0}$ and $\dot{\boldsymbol{F}}\neq\boldsymbol{0}$, an entropic cooling at tension and heating at compression is present at $\boldsymbol{x}\in\mathcal{B}_t$ and, if $\dot{\bar{\boldsymbol{F}}}^{v}\neq\boldsymbol{0}$ and $\dot{\boldsymbol{F}}\neq\boldsymbol{0}$, the temperature is increased as time elapses.

19.3.2 Creep Law

Having Eq. (19.7) at hand, the viscous evolution operator $\bar{\boldsymbol{L}}^{v}$ related to the viscous intermediate configuration, needs to be defined. The standard arguments for defining work conjugates at the intermediate configuration are the positiveness of the internal dissipation, see e.g. [15]. If $\rho_0 \psi^{e}_{iso}(\bar{\boldsymbol{C}}^{e})$ represents the change of energy stored due to viscoelastic loading, the internal dissipation can be defined by

$$\mathcal{D}_{\text{int}} := \mathcal{P} - \rho_0 \dot{\psi}^{e}_{iso}(\bar{\boldsymbol{C}}^{e}) \geq 0 \,, \tag{19.21}$$

where no temperature change is assumed while viscous evolution. The stress power $\mathcal{P} := \bar{\boldsymbol{\Sigma}} : \bar{\boldsymbol{L}}$, as a function of the MANDEL stress

$$\bar{\boldsymbol{\Sigma}} = 2\bar{\boldsymbol{C}}^{e} \frac{\partial \rho_0 \psi^{e}_{iso}(\bar{\boldsymbol{C}}^{e})}{\partial \bar{\boldsymbol{C}}^{e}} \tag{19.22}$$

with respect to the intermediate configuration, is introduced, see [1]. The total rate of deformation $\bar{\boldsymbol{L}} = \bar{\boldsymbol{F}}^{e} \bar{\boldsymbol{l}} \bar{\boldsymbol{F}}^{e^{-1}}$ related to the intermediate configuration can be split into

$$\bar{\boldsymbol{L}} = \bar{\boldsymbol{L}}^{e} + \bar{\boldsymbol{L}}^{v} \,, \tag{19.23}$$

where $\bar{\boldsymbol{L}}^{e} = \bar{\boldsymbol{F}}^{e^{-1}} \dot{\bar{\boldsymbol{F}}}^{e}$, compared to [6]. A further evaluation of Eq. (19.21) yields

$$\rho_0 \dot{\psi}^{e}_{iso}(\bar{\boldsymbol{C}}^{e}) = \frac{\partial \rho_0 \psi^{e}_{iso}(\bar{\boldsymbol{C}}^{e})}{\partial \bar{\boldsymbol{C}}^{e}} : \dot{\bar{\boldsymbol{C}}}^{e} = \left[2\bar{\boldsymbol{C}}^{e} \frac{\partial \rho_0 \psi^{e}_{iso}(\bar{\boldsymbol{C}}^{e})}{\partial \bar{\boldsymbol{C}}^{e}} \right] : \bar{\boldsymbol{L}}^{e} \,, \tag{19.24}$$

for the inelastic and isochoric part of the HELMHOLTZ energy. Inserting Eq. (19.23) and Eq. (19.24) into Eq. (19.21) and applying the standard arguments for the strict positiveness of the internal dissipation leads to the constitutive description of $\bar{\boldsymbol{\Sigma}}$ (compare Eq. (19.22)), reading

$$\mathcal{D}_{\text{int}} := \left[\bar{\boldsymbol{\Sigma}} - 2\bar{\boldsymbol{C}}^{e} \frac{\partial \rho_0 \psi^{e}_{iso}(\bar{\boldsymbol{C}}^{e})}{\partial \bar{\boldsymbol{C}}^{e}} \right] : \bar{\boldsymbol{L}} + \left[2\bar{\boldsymbol{C}}^{e} \frac{\partial \rho_0 \psi^{e}_{iso}(\bar{\boldsymbol{C}}^{e})}{\partial \bar{\boldsymbol{C}}^{e}} \right] : \bar{\boldsymbol{L}}^{v} \geq 0 \,. \tag{19.25}$$

The following constitutive definition for $\bar{\boldsymbol{L}}^{v}$ is introduced, reading

$$\bar{\boldsymbol{L}}^{v} := \dot{\gamma}^{v} \boldsymbol{N} = \dot{\gamma}^{v} \frac{\bar{\boldsymbol{\Sigma}}}{\|\bar{\boldsymbol{\Sigma}}\|} \,. \tag{19.26}$$

Compare [16], the creep flow is defined as

$$\dot{\gamma}^{v} = \dot{\gamma}_0 \left[\exp\left(\left(\frac{\|\boldsymbol{\Sigma}\|}{s_0} \right)^{n} \right) - 1 \right] \,, \tag{19.27}$$

where $\dot{\gamma}_0$ denotes the pre-exponential shear strain rate factor. n and s_0 are another two material parameters. Here, both of them are given as constant coefficients. It ensures the inequality of internal dissipation, see Eq. (19.25). Recalling Eq. (19.7), the time integration is given by

$$\dot{\bar{\boldsymbol{F}}}^{v} = \left[\dot{\gamma}^{v}\boldsymbol{N}\right]\bar{\boldsymbol{F}}^{v} \,. \tag{19.28}$$

Within a standard time discretization, the implicit update algorithm

$$\bar{\boldsymbol{F}}^{v}_{n+1} = \exp\left[\Delta\gamma^{v}_{n+1}\boldsymbol{N}_{n+1}\right]\bar{\boldsymbol{F}}^{v}_{n} \,, \tag{19.29}$$

is applied for a time increment $\{t_n, t_{n+1}\} \in \mathbb{R}$ as an approximation.

19.3.3 Governing Equations

This section briefly summarizes the spatial formulation of the driving partial differential equations (PDE) for evolving the global nodal unknowns, i.e. temperature, displacements, velocities and accelerations. The local forms, where local means the validity at any $\boldsymbol{x} \in \mathcal{B}_t$, are given by

$$\rho\ddot{\boldsymbol{u}} = \rho\boldsymbol{b} + \operatorname{div}(\boldsymbol{\sigma}) \,, \tag{19.30}$$

$$\rho c\dot{\theta} = -\operatorname{div}(\boldsymbol{q}) + \rho\left(\theta \cdot 2\frac{\partial^2\psi}{\partial\boldsymbol{g}\partial\theta}\right) : \boldsymbol{d} - \rho\left(\frac{\partial\psi}{\partial\bar{\boldsymbol{F}}^{v}} - \theta\frac{\partial^2\psi}{\partial\bar{\boldsymbol{F}}^{v}\partial\theta}\right) : \dot{\bar{\boldsymbol{F}}}_{v} \tag{19.31}$$

$$= -\operatorname{div}(\boldsymbol{q}) + \rho w_{\text{ext}} - \rho w_{\text{int}} \,. \tag{19.32}$$

The focus of the contribution at hand is a consistent solution of the path dependent problem by use of a NEWTON-type solver considering initial condition at t_0 for all $\boldsymbol{X} \in \mathcal{B}_0$ and boundary conditions for all $\boldsymbol{x} \in \mathcal{B}_t$ and $\boldsymbol{X} \in \mathcal{B}_0$. The boundary of B is divided into $\partial B = \{\partial B_u \,,\, \partial B_\theta\} = \{\partial B_\sigma \,,\, \partial B_q\}$, compare Fig. 19.1, with prescribed displacements, temperatures or tractions and heat flows for each of the configurations.

19.4 Numerical Study

In this section, a numerical example is conducted in comparison with the related experimental investigation, in order to intuitively demonstrate the capability of the present model. Based on [5], a flat specimen of polyoxymethylene (POM) with stress-controlled load and strain-controlled load is modeled, respectively. The material constants are shown in Table 19.1 The specimen geometry is depicted in Fig. 19.2 (a) and the finite element discretization is shown in Fig. 19.2 (b).

Table 19.1: Material parameters.

κ	μ	α_t	k_t	$\rho_0 c$	θ_0	$\dot{\gamma}_0$	s_0	n
2000 MPa	110 MPa	$2e^{-3}$	0.3 N/s·K	2 N/(mm^2·K)	333 K	$7.5e^{-9}$	12.5 MPa	2.37

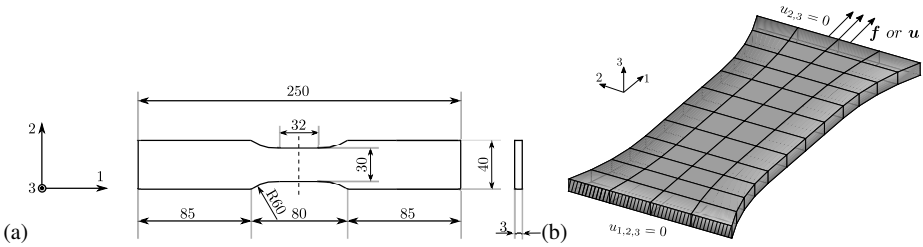

Fig. 19.2: (a) geometry of the flat specimen with all measures in mm; (b) setup for finite element model.

19.4.1 Stress-Controlled loading

In the stress-controlled loading simulation, a set of nominal stresses $\sigma = \{27.5, 30, 33, 35\}$MPa is considered, which can be mimicked alternatively by applying a force $\boldsymbol{f}$ to yield a same level of stress in the cross-section of the central region in the specimen, see Fig. 19.2 (b). The longitudinal strain $\varepsilon_1 = \ln(l/l_0)$ and lateral strain $\varepsilon_2 = \ln(\omega/\omega_0)$ in a logarithmic formulation are two essential parameters for analyzing the experimental outcomes. Hence, in the numerical evaluation, a similar behavior is obtained for an effective comparison.

In comparison with experimental outcomes from [5], the simulation results by the present model based on a stress-controlled loading are validated in Fig. 19.3 with respect to all the stress states $\{27.5, 30, 33, 35\}$ MPa. It can be evidently seen that the numerical prediction shows a good agreement to the experimental investigation for all setups. Furthermore, the model also captures the characteristic that the strain growth rate increases obviously with the larger nominal stress application. Therefore, the given creep law in Eq. (19.27) is demonstrated to have a good performance in fitting the overall experimental results.

Furthermore, the deformation process with the nominal stress $\sigma = 33$ MPa is also shown in Fig. 19.4 for a straightforward visualization of the creep behavior. Considering the original length 80 mm, the creep deformation is obviously observed as time increases, e.g., it reaches more than 100 mm at $t = 1.78\text{e}^4$ s. In addition, the temperature evolution along the time is investigated. Figure 19.5 depicts the temperature change ϑ in the central point of the specimen along the time increase.

Moreover, another interesting comparison about temperature evolution is shown in Fig. 19.6, which describes the temperature distribution for all nominal stress applications but at the same specimen elongation state.

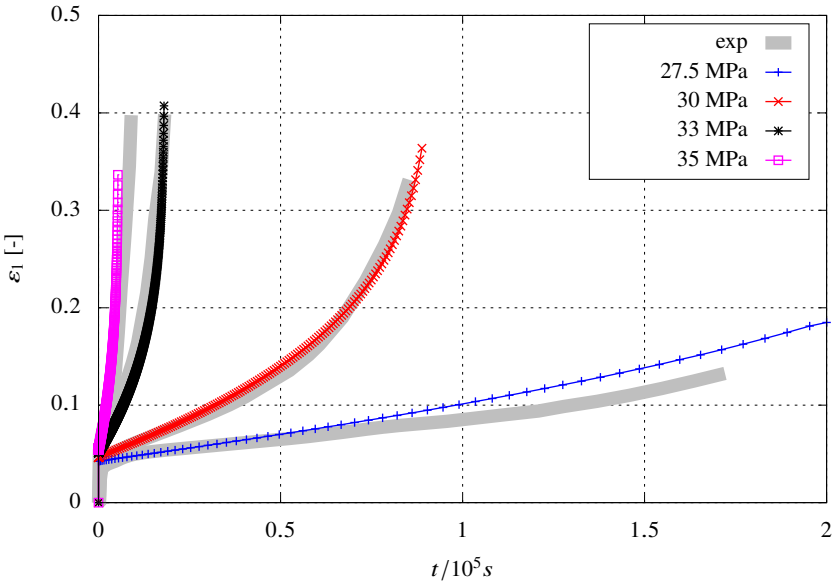

Fig. 19.3: Model results under stress-controlled loading.

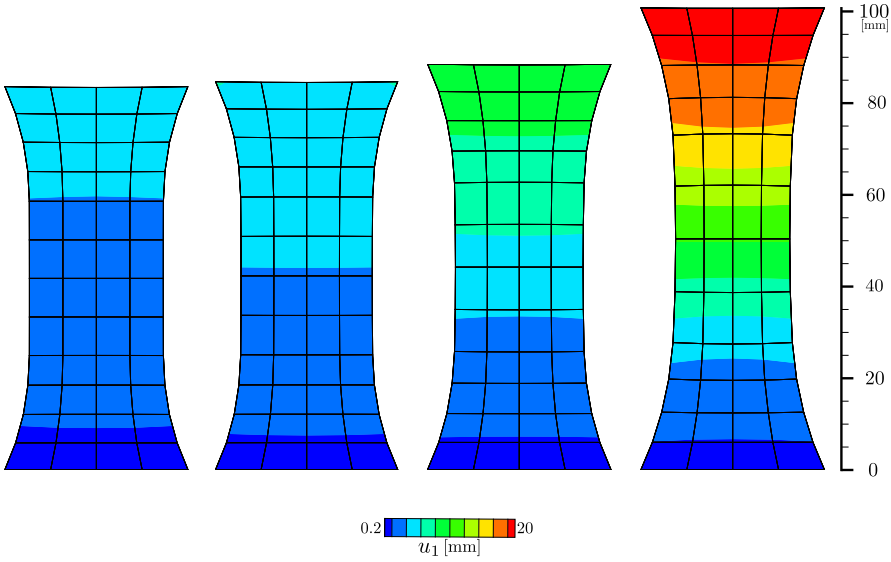

Fig. 19.4: Creep deformation of the numerical model at $t = [10, 4.3\text{e}^3, 1.12\text{e}^4, 1.78\text{e}^4]$ s with $\sigma = 33$ MPa.

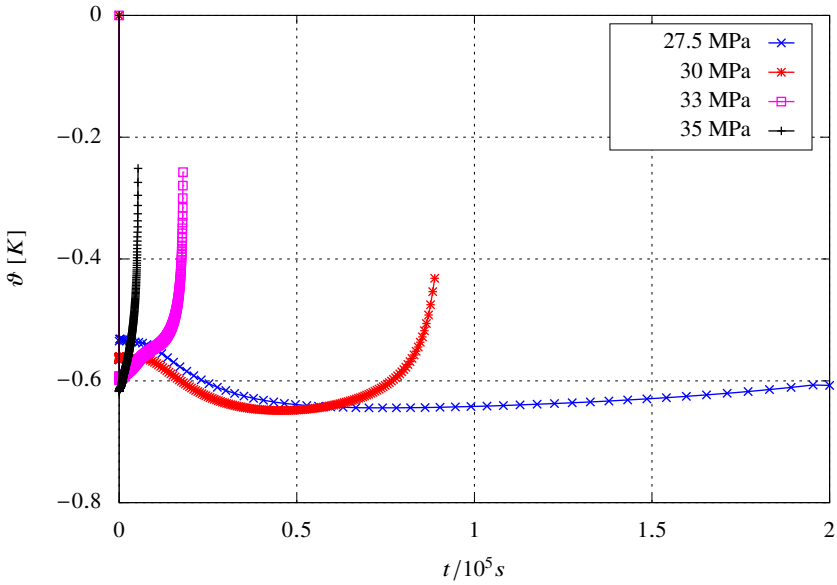

Fig. 19.5: Temperature course in the central point of specimen under stress-controlled loading.

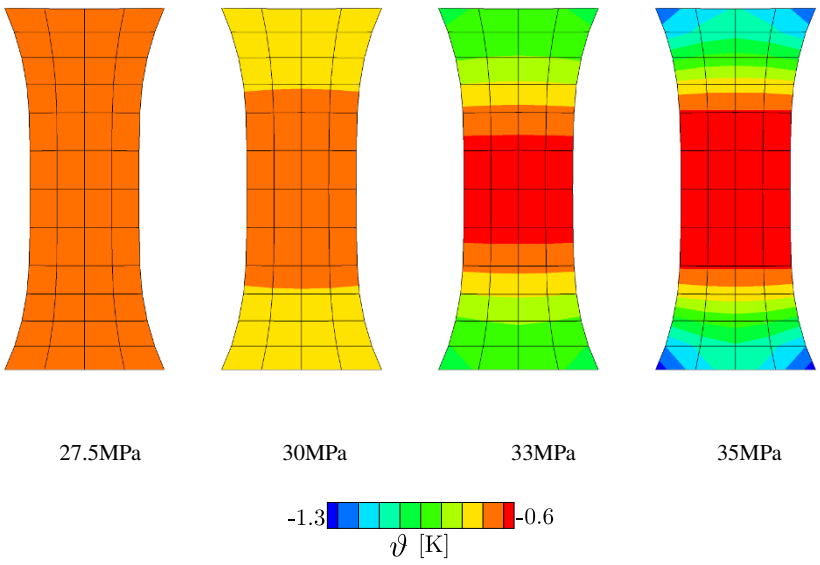

Fig. 19.6: Temperature distribution of the flat specimen with the stain state $\varepsilon_1 = 0.185$ under stress-controlled loading.

19.4.2 Strain-Controlled loading

The strain-controlled tension test is experimentally conducted by SCHLEGEL & BEINER. For the detail of experimental setup, one is referred to [5, 17]. As shown in Fig. 19.2, the same material constants, the same specimen geometry and finite element model are used with the only difference being the load application. The applied strain rate is determined from the free length of the specimen between the clamps. Herein, a machine speed of $v = 0.8$ mm/min for a global strain rate $\dot{\varepsilon} = 0.01$ min^{-1} and $v = 8$ mm/min for $\dot{\varepsilon} = 0.1$ min^{-1} approximation are used. With respect to the experiment, results in the following are presented with the nominal strain definition $\varepsilon_1 = l/l_0 - 1$ for the longitudinal strain and $\varepsilon_2 = \omega/\omega_0 - 1$ for the lateral strain. Nominal stress σ is again given by measured force divided by the initial size of the middle cross-section of the specimen.

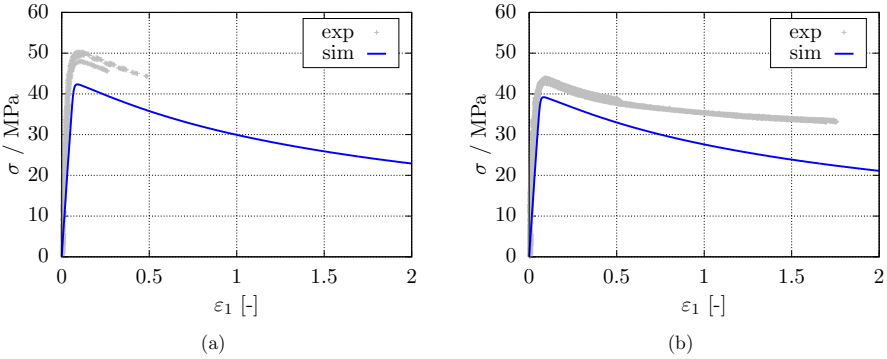

Fig. 19.7: Longitudinal results for tension tests with strain rates:
(a) $\dot{\varepsilon} = 0.1\text{min}^{-1}$; (b) $\dot{\varepsilon} = 0.01\text{min}^{-1}$.

Results from the tension tests with two different strain rates are illustrated in Fig. 19.7. Experiments show an initially stiff response until a nominal stress maximum σ_{crit} is reached. In the sequel, significant softening is observed until rupture. The simulation results match the experimental results during the initially stiff phase. Nevertheless, the peak stresses are unfortunately not appropriately predicted, which yields an underestimation of the peak stress values. The possible reasons behind it can be from the material constants fitting, as well as the measurement deviations. But the good side is that the softening trends for both cases are also similar to the experimental results. Therefore, further efforts, from both the experimental measurements and model fitting aspects, are certainly required to overcome such imperfect predictions.

19.5 Summary

The developments presented in this contribution successfully introduces a stable and robust modeling approach to simulate a class of thermo-viscoelastic materials at finite deformations. This is achieved by a consistent numerical framework, which is introduced with respect to the linearization of the global and local driving evolution equations. The constitutive descriptions, such as the presented HELMHOLTZ energy or the creep law, are examples. Herein, the applicability of the aforementioned formulations is demonstrated mainly for polymeric materials. Nevertheless, it can be easily exchanged to other materials, e.g., when thermo-plastic materials are required to be modeled. Further physical validation with respect to temperature changes and larger deformations of other classes of inelastic materials or composites is certainly possible. Additionally, other multi-physical phenomena can also be properly addressed by considering further multiplicative splits of the deformation gradient.

References

[1] Miehe C (1992) Kanonische Modelle multiplikativer Elasto-Plastizität. Thermodynamische Formulierung und numerische Implementation. Habilitation thesis, Universität Hannover
[2] Fleischhauer R, Platen J, Kato J, Terada K, Kaliske M (2022 (under review)) A finite anisotropic thermo-elasto-plastic modeling approach to additive manufactured specimens. Engeneering Computations
[3] Zerbe P, Schneider B, Moosbrugger E, Kaliske M (2017) A viscoelastic-viscoplastic-damage model for creep and recovery of a semicrystalline thermoplastic. International Journal of Solids and Structures **110**:340–350
[4] Miehe C (1988) Zur numerischen Behandlung thermomechanischer Prozesse. Phd thesis, Universität Hannover
[5] Zerbe P (2017) Constitutive modeling of a semicrystalline thermoplastic under cyclic creep loading - Konstitutive Modellierung eines teilkristallinen Thermoplast. Phd thesis, Technische Universität Dresden
[6] Lee EH (1969) Elastic-Plastic Deformation at Finite Strains. Journal of Applied Mechanics **36**:1–6
[7] Moran B, Ortiz M, Shih CF (1990) Formulation of implicit finite element methods for multiplicative finite deformation plasticity. International Journal for Numerical Methods in Engineering **29**:483–514
[8] Lubarda VA (2004) Constitutive theories based on the multiplicative decomposition of deformation gradient: Thermoelasticity, elastoplasticity, and biomechanics. Applied Mechanics Reviews **57**:95–108
[9] Yin B, Kaliske M (2020) Fracture simulation of viscoelastic polymers by the phase-field method. Computational Mechanics **65**:293–309
[10] Yin B (2022) Phase-field fracture description on elastic and inelastic materials at finite strains. Phd thesis, Technische Universität Dresden

[11] Simo JC (1998) Numerical analysis and simulation of plasticity. Handbook of Numerical Analysis **6**:183–499
[12] Kaliske M (2000) A formulation of elasticity and viscoelasticity for fibre reinforced material at small and finite strains. Computer Methods in Applied Mechanics and Engineering **185**:225–243
[13] Fleischhauer R, Thomas T, Kato J, Terada K, Kaliske M (2020) Finite thermo-elastic decoupled two-scale analysis. International Journal for Numerical Methods in Engineering **121**:355–392
[14] Hughes TJR, Marsden JE (1983) Mathematical Foundations of Elasticity. Dover Publications, Inc., New York
[15] Truesdell C, Noll W (2004) The non-linear field theories of mechanics. Springer Berlin, Heidelberg
[16] Boyce MC, Parks DM, Argon AS (1988) Large inelastic deformation of glassy polymers. Part I: rate dependent constitutive model. Mechanics of Materials **7**:15–33
[17] Schlegel R, Beiner M (2015) Zyklische Versuche und Zugsversuche an POM mit optischer Dehnungsmessung. Report, Fraunhofer-Institut für Mikrostruktur von Werkstoffen und Systemen IWMS, Halle (Saale)